Chinese Journal of Chemical Engineering 95 (2026) 102–112

Contents lists available at ScienceDirect

Chinese Journal of Chemical Engineering

journal homepage: www.elsevier.com/locate/CJChE

Full Length Article

Recovery of calcium resources from phosphogypsum in the preparation of sulfoaluminate cement: Decomposition mechanism and minerals formation

Shuang Wu [1,*], Changzai Ren [2,*], Xingliang Yao [3], Yonggang Yao [4], Wenlong Wang [4]

[1] State Key Laboratory of Green Papermaking and Resource Recycling, Faculty of Light Industry, Qilu University of Technology (Shandong Academy of Sciences), Jinan 250353, China
[2] School of Energy and Power Engineering, Qilu University of Technology, Jinan 250306, China
[3] School of Energy and Power Engineering, North University of China, Taiyuan 030051, China
[4] National Engineering Laboratory for Coal-fired Pollutants Emission Reduction, Shandong University, Jinan 250061, China

ARTICLE INFO

Article history:
Received 23 July 2025
Received in revised form
24 January 2026
Accepted 1 February 2026
Available online 17 April 2026

Keywords:
Phosphogypsum
Decomposition
Sulfoaluminate cement
Minerals formation
Thermodynamics analysis

ABSTRACT

Phosphogypsum (PG) is a solid waste generated by the phosphate fertilizer industry. The decomposition of PG allows for the separate recovery of its Ca and S resources. In this work, the decomposition of PG and formation of minerals in the preparation of sulfoaluminate cement (SAC) were studied. Thermodynamics analysis reveals that the formation of SAC minerals accelerates the decomposition of PG by incorporating $CaSO_4$ and CaO into the reaction matrix. Experimental results revealed that the formation of SAC minerals effectively reduces the decomposition temperature of PG and increases its decomposition rate. The formation of C_2S has the strongest promoting effect on the decomposition of PG. The formation of $C_4A_3\overline{S}$ generally has a weaker effect in promoting PG decomposition. In contrast, the formation of C_4AF and composite minerals not only facilitates efficient PG decomposition but also maintains system stability, preventing melting. The formation of SAC minerals is affected by the decomposition of PG, making it difficult to fully generate the target mineral. The kinetic mechanism of PG decomposition is three-dimensional diffusion reaction, while the mechanism changes to two-dimensional diffusion (cylindrical symmetry) reaction in mineral formation. This study presents novel methodologies for recycling Ca and S resources from PG, paving the way for its efficient utilization.
© 2026 The Chemical Industry and Engineering Society of China, and Chemical Industry Press Co., Ltd. All rights are reserved, including those for text and data mining, AI training, and similar technologies.

1. Introduction

Although the phosphate fertilizer industry holds immense economic significance, it is widely regarded as one of the most polluting industries globally [1]. This industrial activity is characterized by its diverse and hazardous emissions to air, liquids and solid wastes [2]. Phosphogypsum (PG) is a waste byproduct generated from the wet process of phosphoric acid in the phosphate fertilizer industry [3]. Producing one ton of phosphoric acid yields approximately 4.0–5.0 tons of PG [4]. According to statistics, approximately 300 million tons of PG are produced annually worldwide [5]. Currently, about 15% of PG is recycled and reused, such as for agricultural fertilizer, saline soil conditioner, road construction, building materials, etc [6]. Most of the PG is stored as solid waste without any treatment. This instance occupies land and harms the environment, but also causes waste of Ca and S resources [7]. Therefore, finding solutions for the recycling of PG has become an urgent priority.

The main component of PG is calcium sulfate dihydrate ($CaSO_4 \cdot 2H_2O$), which is rich in Ca and S resources [8]. One of the main ways to utilize PG is to separately recover Ca and S resources. The SO_2 obtained by the decomposition of PG can be converted into element S or made into sulfuric acid [9]. Element S is an important raw material for many manufacturing industries, such as fertilizers [10], acids [11], insecticides [12], and titanium dioxide [13]. Ca also has many uses in various industrial and commercial applications, such as manufacturing concrete or Portland cement

* Corresponding authors.
E-mail addresses: wus130708@163.com (S. Wu), rcz@qlu.edu.cn (C. Ren).

https://doi.org/10.1016/j.cjche.2026.02.012
1004-9541/© 2026 The Chemical Industry and Engineering Society of China, and Chemical Industry Press Co., Ltd. All rights are reserved, including those for text and data mining, AI training, and similar technologies.

[14], producing lime for soil stabilization [15], acid neutralization [16], and flue gas desulfurization [17]. The decomposition process of PG has attracted the attention of many scholars. PG can be decomposed into CaO and SO_2 through high-temperature calcination, achieving its effective recovery [18]. But high-temperature decomposition is not economical. The addition of reducing agents can effectively reduce the decomposition temperature and improve the decomposition efficiency of PG [19]. The mechanism of PG reductive decomposition is currently unclear, and the reaction process is difficult to control [20]. CaO, CaS, and $CaSO_4$ are usually mixed in the product, making it difficult to achieve high purity of the target product [21,22]. Therefore, it is quite difficult to effectively separate Ca and S resources through the reductive decomposition of PG.

Some studies have shown that the decomposition of PG can be promoted by oxides such as Al_2O_3, Fe_2O_3, SiO_2, *etc.* [23–25]. In addition to catalytic effects, the mineral formation reaction between oxides and CaO further facilitates the decomposition of PG. Our team successfully prepared sulfoaluminate cement (SAC) using PG as the sole CaO source based on this phenomenon [26,27]. The obtained SAC has good mineral formation and excellent performance. The efficient decomposition of PG meets the demand for the co-production of sulfuric acid with SAC [28]. During the preparation of SAC, CaO reacts with Al_2O_3, SiO_2, and Fe_2O_3 to form clinker minerals such as ye'elimite ($C_4A_3\overline{S}$), belite (C_2S), and brownmillerite (C_4AF) [29]. At this point, the decomposition of PG is effectively promoted. However, the promoting effect of different mineral formations on PG decomposition is not clear. And the mineral formation process involving PG decomposition is still unknown.

This work investigated the decomposition of PG and formation of minerals in the preparation of SAC. From a thermodynamic perspective, the decomposition reaction of PG and the formation of clinker minerals such as $C_4A_3\overline{S}$, C_2S, and C_4AF from PG were analyzed. The decomposition behavior of PG and the formation of SAC clinker minerals were explored through methods such as thermogravimetric analysis-mass spectrometry (TG-MS) and X-ray diffraction (XRD). And the microstructure evolution during the decomposition of PG and minerals formation was observed using scanning electron microscopy (SEM). The decomposition kinetics mechanism of PG at high temperatures was revealed. This work provides important theoretical support and insights for the innovative recovery of Ca and S resources in PG.

2. Experiments

2.1. Sample preparation

The PG used in the work comes from the Shandong Huitai Co., Ltd., Binzhou, China. Through chemical composition analysis of PG, it contains 36.78% (mass) CaO, 51.75% (mass) SO_3, and 5.17% (mass) SiO_2, as well as a small amount of Al_2O_3, Fe_2O_3, MgO and other components. The chemical compositions of PG are presented in Table 1. The XRD pattern of PG is shown in Fig. 1. The main mineral of PG is $CaSO_4\cdot 2H_2O$. The Al_2O_3, SiO_2, and Fe_2O_3 used in the work are all chemically pure reagents from China National Pharmaceutical Group Co., Ltd. The proportion of raw materials is based on the predetermined target mineral types and contents. Al_2O_3 is added to PG to prepare $C_4A_3\overline{S}$. SiO_2 is added to PG to prepare C_2S. Preparation of C_4AF by reaction of PG with Al_2O_3 and Fe_2O_3. The raw material proportion and corresponding target minerals are shown in Table 2. According to the types of raw materials, the samples are named PGA, PGS, PGAS, and PGASF. PG serves as the reference group and is named PG0.

Table 1
Chemical composition of PG, % (mass).

Sample	CaO	SiO_2	Al_2O_3	Fe_2O_3	SO_3	MgO	TiO_2	R_2O[a]	LOI[b]
PG	36.78	5.17	0.43	0.21	51.75	0.17	0.09	0.19	5.21

[a] Alkaline oxide (K_2O and Na_2O).
[b] Loss on ignition at 950 °C.

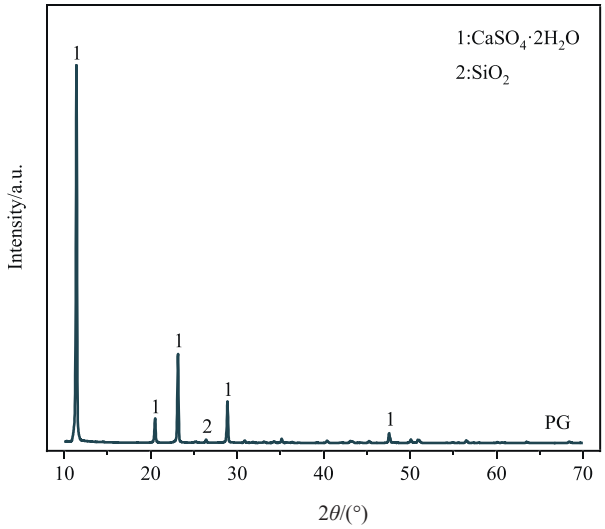


Fig. 1. XRD pattern of the PG sample.

The raw materials are thoroughly mixed according to the predetermined ratio. Then, it was compressed into a cylindrical shape with a diameter of 50 mm under a static pressure of 15 MPa. The uniformly mixed samples were placed at temperatures of 900 °C, 950 °C, 1000 °C, 1050 °C, 1100 °C, 1150 °C, 1200 °C, 1250 °C, 1300 °C and calcined for 60 min. The calcined sample was ground to below 200 mesh for further testing.

2.2. Methods

The thermal decomposition behavior and product generation of PG and other samples were studied using a thermogravimetric analyzer (TGA, NETZSCH STA 449 F3 Jupiter) coupled with a mass spectrometer (MS, QMS 403 Aeolos Quadro). The sample mass in the alumina crucible is maintained at (5 ± 0.5) mg in each experiment. Air is used as the carrier gas, with a flow rate set at 60 ml $\cdot min^{-1}$. The sample is heated from 30 °C to 1200 °C at a heating rate of 10 °C$\cdot min^{-1}$. The gas delivery device between TGA and MS is heated to 200 °C to avoid condensation of gaseous products. MS is used to study the dynamics of gas emissions (H_2O, CO_2, SO_2 and SO_3). All experiments were conducted at least twice to demonstrate good repeatability and reproducibility of the testing.

Elemental analysis was performed using an energy-dispersive X-ray fluorescence spectrometer (XRF, SPECTRO XEPOS). The instrument was equipped with a high-resolution silicon drift detector and operated under optimized measurement conditions for

Table 2
Raw material proportion and corresponding target minerals (% (mass)).

Sample	Target minerals			Raw material proportion			
	$C_4A_3\overline{S}$	C_2S	C_4AF	PG	Al_2O_3	SiO_2	Fe_2O_3
PGA	100	/	/	66.92	33.08	/	/
PGS	/	100	/	83.76	/	16.24	/
PGAF	/	/	100	70.26	11.58	/	18.16
PGAS	70	30	/	73.28	20.58	6.13	/
PGASF	60	30	10	68.38	24.25	5.61	1.76

precision analysis. Measurements were carried out under vacuum conditions using an excitation voltage of 50 kV. Prior to analysis, samples were oven-dried at 110 °C for 2 h. And an appropriate amount of the sample was pressed into a round tablet (5 mm in thickness and 25 mm in diameter) with boric acid for testing. Each measurement was performed in triplicate to confirm reproducibility.

The decomposition rate of PG is calculated based on the mass and SO_3 content of the sample before and after calcination, as shown below [30].

$$\text{Decomposition rate}\ (\%) = \frac{M_1 \times S_1 - M_2 \times S_2}{M_1 \times S_1}$$

here, M_1 and S_1 represent the mass and SO_3 content of the sample after eliminating ignition loss, respectively, and M_2 and S_2 correspond to the mass and SO_3 content of the calcined sample, respectively.

The mineral composition of the calcined sample was analyzed using a XRD X-ray diffraction analysis (XRD, Brucker Advance D8) equipped with a Cu-K_α radiation source (λ = 0.15406 nm). The sample test voltage and current of the X-ray tube were set at 40 kV and 40 mA, respectively. The measurements are conducted within the 2θ range of 10° to 80° with a scanning speed of 0.2(°)·min^{-1}. A LynxEye detector was used to collect the signals. Table 3 shows the crystal structures used for analysis and corresponding Inorganic Crystal Structure Database (ICSD) codes.

The morphology and microstructural analysis of the samples were conducted using a scanning electron microscope (SEM, Zeiss Supra 55) operated at an accelerating voltage of 5 kV. Prior to imaging, the samples were sputter-coated with a thin layer of gold to enhance conductivity and minimize charging effects. The high-vacuum mode was employed throughout the analysis.

FactSage is a powerful thermodynamic software package used to simulate and analyze chemical reactions [40]. To determine whether a chemical reaction will occur, the Gibbs free energy ΔG of the system under specific conditions such as temperature, pressure, and composition is calculated. A reaction is considered thermodynamically favorable if Gibbs free energy ΔG is negative, indicating that the process can proceed spontaneously [41]. In this study, the "Reaction" module of FactSage 7.1 was used to obtain the relationship between the Gibbs free energy ΔG of chemical reactions and temperature [42]. The evaluated reactions included the decomposition of PG and its interactions with various oxides. Calculations were performed over a temperature range of 400 °C–2000 °C with increments of 100 °C. The resulting data were subsequently organized and plotted for analysis.

3. Results and Discussion

3.1. Thermodynamic analysis

The reactions that occur during the decomposition of PG in different systems were summarized, as shown in reactions (1–16).

Table 3
Crystal structures used for analysis and ICSD codes.

Mineral name	Formula	ICSD codes
Anhydrite	$C\overline{S}$	15876 [31]
Silica	SiO_2	67121 [33]
Krotite	CA	260 [35]
Wollastonite	CS	26553 [37]
Brownmillerite	C_4AF	9197 [39]
Gehlenite	C_2AS	87144 [32]
Srebrodolskite	C_2F	15059 [34]
Ye'elimite	C_4A_3S	9560 [36]
Belite	C_2S	81096 [38]

In the PG0 sample, the main reactions that occur are the dehydration of $CaSO_4 \cdot 2H_2O$ and the decomposition of $CaSO_4$, which can be represented by reactions (1–2).

$$CaSO_4 \cdot 2H_2O\ (s) \rightarrow CaSO_4\ (s) + 2H_2O\ (g) \quad (1)$$

$$2CaSO_4\ (s) \rightarrow 2CaO\ (s) + 2SO_2\ (g) + O_2\ (g) \quad (2)$$

In the PGA samples, $C_4A_3\overline{S}$ and $CaAl_2O_4$ (CA) are formed through different pathways, which can be represented by reactions (3–6).

$$8CaSO_4\ (s) + 6Al_2O_3\ (s) \rightarrow 2Ca_4Al_6SO_{16}\ (s) + 6SO_2\ (g) + 3O_2\ (g) \quad (3)$$

$$3CaO\ (s) + 3Al_2O_3\ (s) + CaSO_4\ (s) \rightarrow Ca_4Al_6SO_{16}\ (s) \quad (4)$$

$$2CaSO_4\ (s) + 2Al_2O_3\ (s) \rightarrow 2CaAl_2O_4\ (s) + 2SO_2\ (g) + O_2\ (g) \quad (5)$$

$$CaO\ (s) + Al_2O_3\ (s) \rightarrow CaAl_2O_4\ (s) \quad (6)$$

In the PGS samples, C_2S and $CaSiO_3$ (CS) are formed, as shown in reactions (7–10).

$$2CaSO_4\ (s) + 2SiO_2\ (s) \rightarrow 2CaSiO_3\ (s) + 2SO_2\ (g) + O_2\ (g) \quad (7)$$

$$CaO\ (s) + SiO_2\ (s) \rightarrow CaSiO_3\ (s) \quad (8)$$

$$4CaSO_4\ (s) + 2SiO_2\ (s) \rightarrow 2Ca_2SiO_4\ (s) + 4SO_2\ (g) + 2O_2\ (g) \quad (9)$$

$$2CaO\ (s) + SiO_2\ (s) \rightarrow Ca_2SiO_4\ (s) \quad (10)$$

In the PGAF samples, not only C_4AF will form, but also $C_4A_3\overline{S}$ and $Ca_2Fe_2O_5$ (C_2F) will form. The reactions involved can be represented by reactions (11–14).

$$2CaSO_4\ (s) + Fe_2O_3\ (s) \rightarrow Ca_2Fe_2O_5\ (s) + 2SO_2\ (g) + O_2\ (g) \quad (11)$$

$$2CaO\ (s) + Fe_2O_3\ (s) \rightarrow Ca_2Fe_2O_5\ (s) \quad (12)$$

$$4CaSO_4\ (s) + Al_2O_3\ (s) + Fe_2O_3\ (s) \rightarrow Ca_4Al_2Fe_2O_{10}\ (s) + 4SO_2\ (g) + 2O_2\ (g) \quad (13)$$

$$4CaO\ (s) + Al_2O_3\ (s) + Fe_2O_3\ (s) \rightarrow Ca_4Al_2Fe_2O_{10}\ (s) \quad (14)$$

In the PGAS samples, in addition to the formation of $C_4A_3\overline{S}$ and C_2S, $Ca_2Al_2SiO_7$ (C_2AS) is also generated, which can be represented by reaction (15–16).

$$2CaSO_4\ (s) + Al_2O_3\ (s) + SiO_2\ (s) \rightarrow Ca_2Al_2SiO_7\ (s) + 2SO_2\ (g) + O_2\ (g) \quad (15)$$

$$2CaO\ (s) + Al_2O_3\ (s) + SiO_2\ (s) \rightarrow Ca_2Al_2SiO_7\ (s) \quad (16)$$

Thermodynamic analysis can not only predict whether a reaction occur and the conditions required for it to occur, but also predict the phase composition of the product at the equilibrium of the reaction. Fig. 2 shows the Gibbs free energy ΔG of $CaSO_4$ decomposition and minerals formation as a function of temperature. Mineral formation reactions can be divided into two categories, one is the reaction in which $CaSO_4$ directly participates in mineral formation, and their Gibbs free energy ΔG is shown in Fig. 2(a). The other type is the reaction in which CaO, a product of PG decomposition, participates in mineral formation, and their Gibbs free energy ΔG is shown in Fig. 2(b). When the temperature reaches 1652 °C, the ΔG of chemical reaction (2) is less than 0,

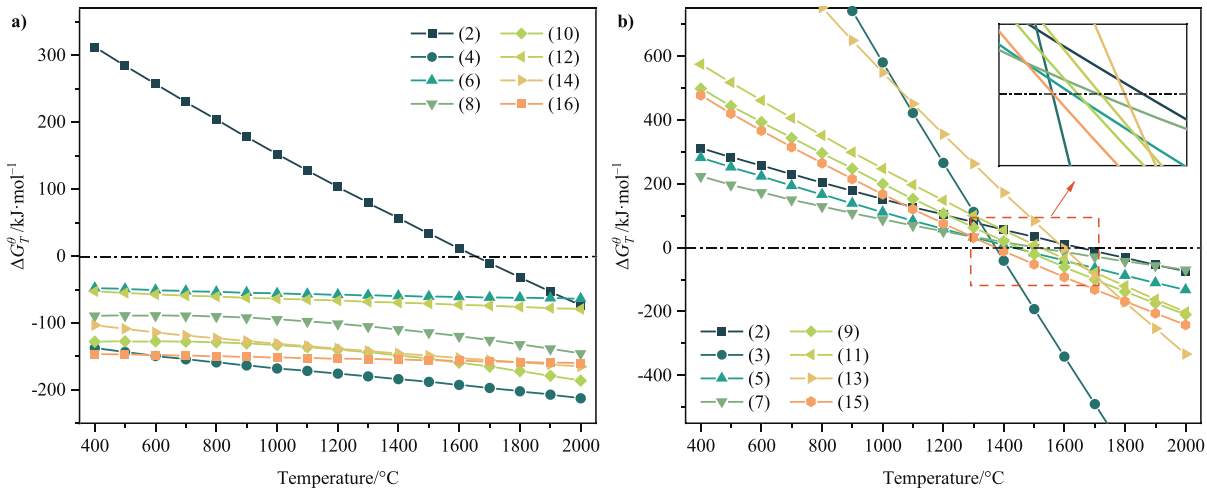


Fig. 2. Gibbs free energy of $CaSO_4$ decomposition and minerals formation (a) mineral formation without $CaSO_4$ decomposition; (b) mineral formation with $CaSO_4$ decomposition.

indicating that $CaSO_4$ can spontaneously decompose. Mineral formation reactions involving CaO can only occur after the decomposition of $CaSO_4$, even though these reactions are thermodynamically spontaneous at relatively low temperatures. In contrast, the mineral formation reactions involving $CaSO_4$ decomposition can proceed directly. At 1373 °C, the ΔG of chemical reaction (3) is less than 0, and $C_4A_3\overline{S}$ spontaneously forms, accompanied by the decomposition of $CaSO_4$. The temperature at which ΔG is less than 0 in chemical reaction (15) is 1375 °C, and C_2AS is formed. Compared with reaction (2), the temperature at which the Gibbs free energy ΔG of minerals formation reactions involving $CaSO_4$ decomposition is below 0 decrease to varying degrees, indicating that mineral formation is more likely to occur spontaneously. The formation of minerals is accompanied by the decomposition of $CaSO_4$ and promotes its decomposition.

3.2. Thermal analysis

Fig. 3 shows the TG-MS curve of PG0 sample. According to the TG-MS curve, the thermal decomposition of PG can be divided into two stages [43]. The initial stage is the dehydration process of PG. PG begins to lose bound water at 90 °C, and as the temperature increases, the dehydration rate gradually increases, reaching a peak at around 130 °C. Subsequently, the dehydration rate gradually decreased, and the dehydration ended at approximately 170 °C. The dehydration of PG is the process in which $CaSO_4 \cdot 2H_2O$ loses bound water and becomes $CaSO_4$, which can be represented by reaction (1). The second stage is the decomposition process of PG. At 970 °C, the sample mass begins to decrease and $CaSO_4$ begins to decompose. As the temperature increases, the decomposition rate begins to increase and reaches its maximum at 1130 °C. When the temperature reaches 1200 °C, the weight loss caused by $CaSO_4$ decomposition is only 4.89% of the original material. The decomposition process of PG involves the decomposition of $CaSO_4$ to produce CaO, SO_2, and O_2, which can be described by reaction (2). The generation of SO_2 during PG decomposition process was not observed on the MS curve, indicating that the decomposition rate of $CaSO_4$ is low.

The TG-MS curve of PGASF sample is shown in Fig. 4. Similar to sample PG0, the thermal analysis process of PGASF sample can be divided into two stages. The initial stage is the dehydration process of PG, which begins at around 90 °C, reaches the maximum dehydration rate at 150 °C, and ends at 180 °C. Subsequently, a

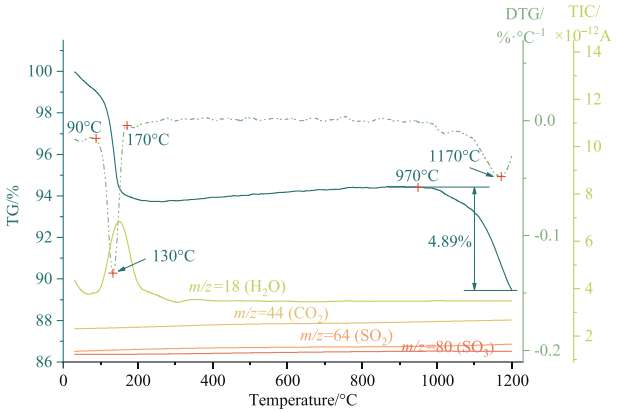


Fig. 3. TG-MS curves of the PG0 samples.

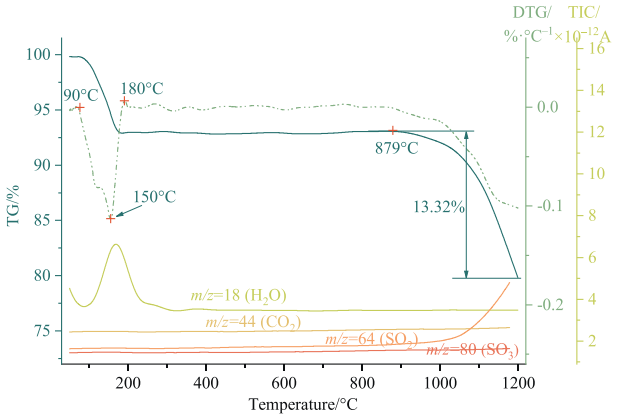


Fig. 4. TG-MS curves of the PGASF sample.

decrease in sample mass was observed at 879 °C, accompanied by the generation of SO_2 on the MS curve, indicating that $CaSO_4$ began to decompose. As the temperature increases, the decomposition rate of PG increases. At 1200 °C, the mass loss caused by the decomposition of $CaSO_4$ is 13.32% of the original material. Compared with the PG0 sample, the initial decomposition temperature of PG decreased by nearly 100 °C, and the mass loss caused by decomposition increased. According to previous studies

[24,26], this behavior was attributed to the catalytic effects of oxides and the formation of minerals, which lower the decomposition temperature of PG and increases its decomposition rate.

3.3. Decomposition rate

To study the effect of mineral formation on the decomposition of PG, the samples were calcined at different temperatures, and some samples were difficult to collect due to melting at 1300 °C, such as PG0 and PGS samples. The decomposition rate of PG in samples sintered at different temperatures is shown in Fig. 5. At 900 °C, the decomposition rate of PG0 sample is 7.02%. As the temperature increases, the decomposition rate gradually rises, reaching 30.30% at 1250 °C. In comparison, other samples exhibit significantly higher decomposition rates. Among them, the PGA sample shows the smallest improvement, with a decomposition rate of 20.78% at 900 °C and 67.67% at 1300 °C. Conversely, the PGS sample demonstrates the greatest improvement, achieving a decomposition rate of 37.42% at 900 °C and 83.49% at 1250 °C. However, at 1300 °C, the system begins to melt due to an increased liquid phase at high temperatures. The PGAF sample achieves the highest decomposition rate at 1300 °C, reaching 86.70%. It can be obtained that the formation of C_2S has the strongest promoting effect on the decomposition of PG, though excessive liquid phase at 1300 °C leads to system melting. The formation of $C_4A_3\overline{S}$ generally has a weaker effect in promoting PG decomposition. In contrast, the formation of C_4AF and composite minerals not only facilitates efficient PG decomposition but also maintains system stability, preventing melting.

3.4. Mineral formation

XRD analysis was performed on the calcined samples to obtain the mineral composition. Fig. 6 shows the XRD patterns of samples sintered at different temperatures. As shown in Fig. 6(a), the PG0 sample contains $CaSO_4$ and SiO_2 after calcination at 800 °C. As the temperature increases, the intensity of the SiO_2 characteristic peak at 26.7° decreases, while that at 28.6° increases, indicating a transformation in its crystal form [44]. However, there was no significant change in the characteristic peak of $CaSO_4$. The characteristic peak of C_2S was observed at 1250 °C. The formation process of C_2S can be described by reaction (9–10), where $CaSO_4$ reacts with SiO_2 to produce C_2S. This means that the $CaSO_4$ has already decomposed to some extent.

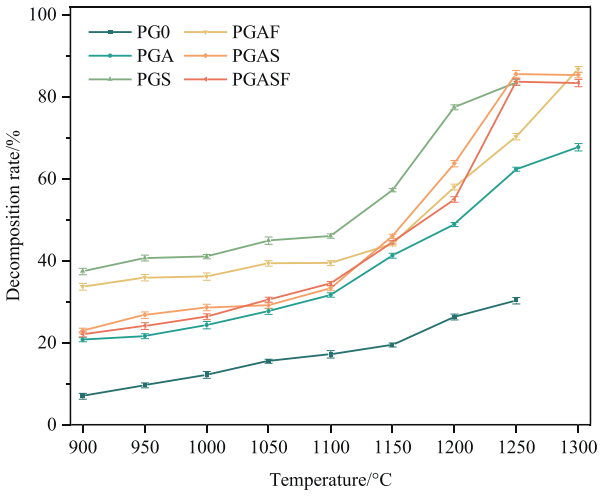


Fig. 5. Decomposition rate of PG in samples sintered at different temperatures.

As shown in Fig. 6(b), the characteristic peak of $C_4A_3\overline{S}$ begins to appear in the PGA sample at 1050 °C, meaning the formation of $C_4A_3\overline{S}$. The formation of $C_4A_3\overline{S}$ can be described by reaction (3–4). This indicates that the reaction is accompanied by the decomposition of $CaSO_4$. With increasing temperature, the intensity of the $C_4A_3\overline{S}$ characteristic peak gradually increases, while that of the $CaSO_4$ peak progressively decreases. At 1300 °C, the characteristic peak of $CaSO_4$ disappears entirely, indicating its complete decomposition. In addition to the target product $C_4A_3\overline{S}$, CA and C_2AS were formed at 1150 °C and 1200 °C, respectively, and their formation processes are described by reactions (5–6) and (15–16).

As shown in Fig. 6(c), $CaSO_4$ and SiO_2 were observed in the PGS sample sintered at 800 °C. At 1000 °C, the characteristic peaks of CS appear, indicating the formation of CS and the decomposition of $CaSO_4$. The formation of CS can be described by reaction (7–8). At 1200 °C, the characteristic peak of C_2S was observed, and C_2S began to form. The formation of C_2S can be represented by reaction (9–10). As the temperature increases, the characteristic peak intensities of CS and C_2S increase, while the characteristic peak intensity of $CaSO_4$ decreases. $CaSO_4$ continues to decompose to form CS and C_2S. At 1300 °C, excessive liquid phase in the system causes the sample to melt. The reason is that SiO_2 and $CaSO_4$ form low melting point silicates, which lower the melting point of the system [45]. Low melting point silicates will gradually melt into a liquid phase with increasing temperature and envelop the reactants, hindering their further reaction. Although SiO_2 is beneficial for the decomposition of PG, it also increases the formation of liquid phase at high temperatures, which can have adverse effects on the further decomposition of PG and the formation of C_2S [46].

In the PGAF sample (Fig. 6(d)), the characteristic peak of $C_4A_3\overline{S}$ begins to appear at 1050 °C and gradually strengthens with increasing temperature. C_2F and C_4AF begin to form at 1250 °C, which can be described by reactions (11–12) and (13–14). At 1300 °C, $CaSO_4$ completely decomposes, and the PGAF sample contains $C_4A_3\overline{S}$, C_4AF and C_2F. The formation temperature of C_4AF is significantly higher than that of $C_4A_3\overline{S}$, resulting in residual $C_4A_3\overline{S}$, and incomplete formation of C_4AF.

Fig. 6(e) shows XRD patterns of PGAS samples sintered at different temperatures. At 1050 °C, $C_4A_3\overline{S}$ formed, accompanied by the decomposition of $CaSO_4$. As the temperature increases, the characteristic strength of $CaSO_4$ weakens and the degree of decomposition increases. At 1150 °C, the characteristic peak of C_2AS can be observed, indicating its formation. At 1200 °C, C_2S has already formed. At 1300 °C, the characteristic peak of $CaSO_4$ disappears entirely, meaning its full decomposition. Due to the absence of $CaSO_4$, C_2AS will not continue to be consumed and remain in the sample [47].

Fig. 6(f) shows XRD patterns of PGASF samples sintered at different temperatures. The mineral evolution process in PGASF samples is similar to that in PGAS samples, with the primary distinction being the increased formation of CS in PGASF. This may be attributed to the promotion of $CaSO_4$ decomposition by Fe_2O_3. Due to the limited addition of Fe_2O_3, the formation of C_4AF was not observed in the samples.

In summary, the formation of SAC minerals promotes the further decomposition of PG by consuming the $CaSO_4$ and CaO produced from it. The formation behavior of minerals reflects their impact on the decomposition of PG. Minerals such as $C_4A_3\overline{S}$, CS, and C_2AS form earlier, effectively promoting the decomposition of PG during the initial phase. In contrast, minerals like CA, C_2S, C_2F, and C_4AF form later, thereby facilitating decomposition of PG in

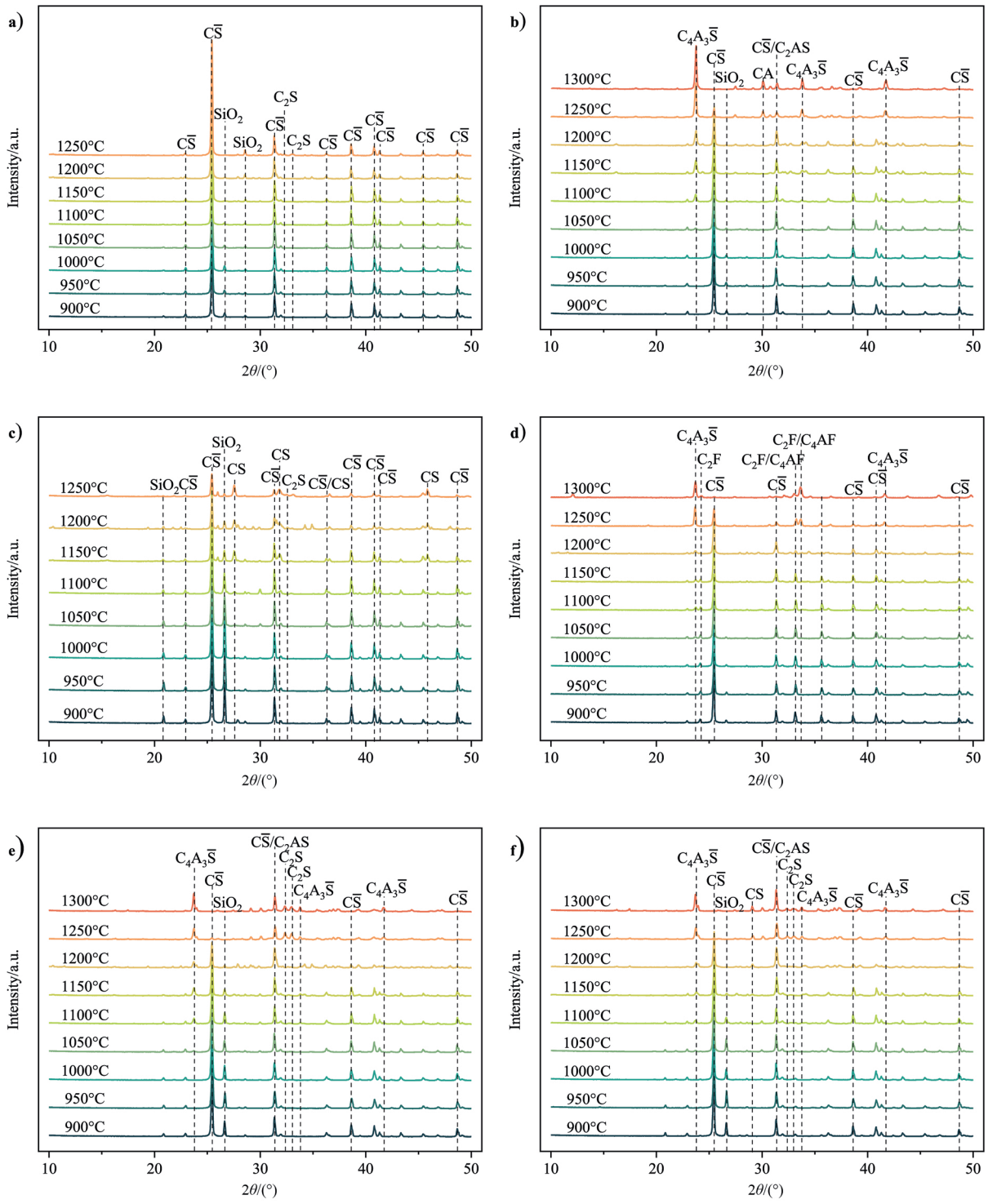


Fig. 6. XRD patterns of samples sintered at different temperatures a) PG0 sample; (b) PGA sample; c) PGS sample; d) PGAF sample; e) PGAS sample; f) PGASF sample.

the subsequent phase. The formation process of SAC minerals is also influenced by the decomposition of PG, which hinders the complete formation of the target minerals.

3.5. Microstructure analysis

To investigate the microstructural evolution during the decomposition of PG, SEM analysis was performed on the calcined samples, and the results are presented in Figs. 7 and 8. Fig. 7 shows the SEM micrographs of PG0 samples sintered at different temperatures. When not calcined, the crystal size of PG is between 100 and 400 μm, and most of them are parallelogram or diamond plate-like shapes. After magnification, it was found that the crystal surface has obvious stacking phenomena, indicating that large crystals are composed of small sheet-like grains stacked together. After calcination at 200 °C, there was no significant change in crystal morphology and size, but due to the loss of bound water, there was a noticeable cracking phenomenon on the surface of the

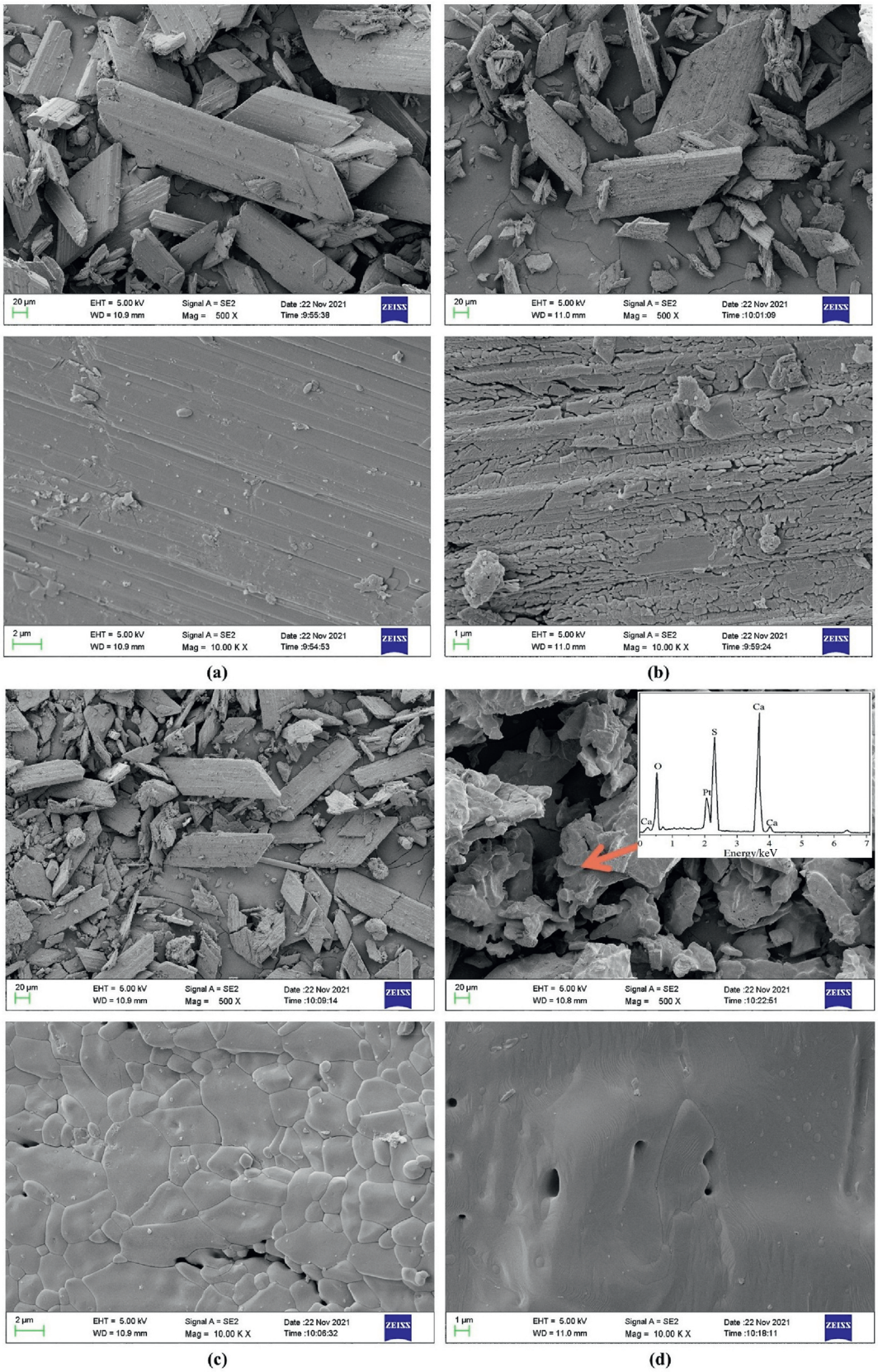


Fig. 7. SEM micrographs of PG0 samples sintered at different temperatures (a) uncalcined; (b) 200 °C; (c) 800 °C; (d) 1200 °C.

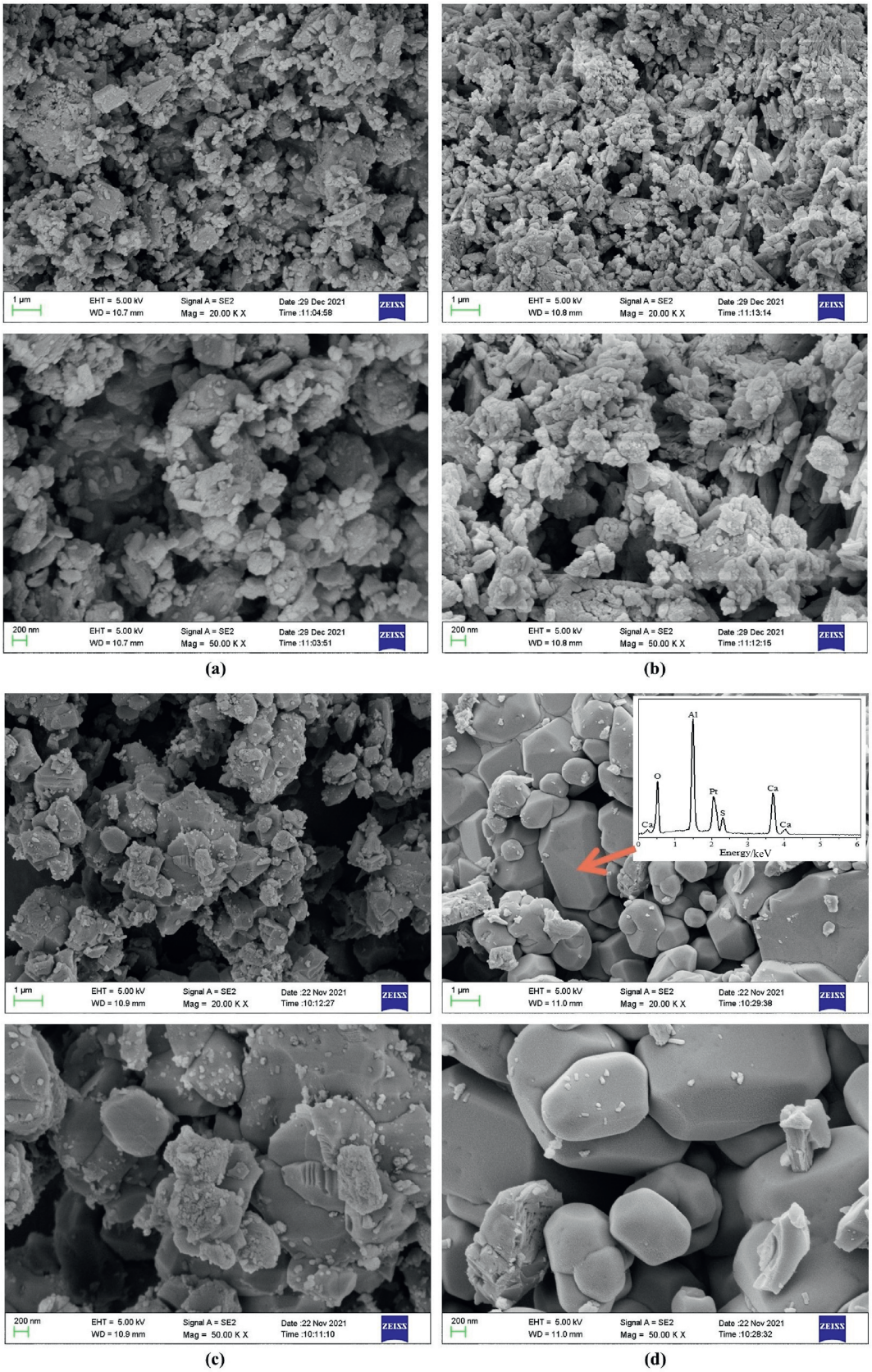


Fig. 8. SEM micrographs of PGASF samples sintered at different temperatures (a) uncalcined; (b) 200 °C; (c) 800 °C; (d) 1200 °C.

crystal. After calcination at 800 °C, the mineral composition is mainly $CaSO_4$. Crystals are mostly in the form of parallelograms or rhomboids, but the original large crystals will break into small-sized crystals, generally between 10 and 120 μm. The surface of the crystal shows a squamous and uneven distribution between grains. After calcination at 1200 °C, the crystals are broken into smaller sizes and exhibit obvious melting phenomena, with rounded edges and smooth surfaces. After magnification, it can be observed that there are no obvious boundaries between the grains, and there are pores generated by gas escape.

Fig. 8 presents the SEM images of PGASF samples sintered at different temperatures. As shown in Fig. 8(a), the regular crystals of the uncalcined sample were destroyed due to pre-grinding. Therefore, the PGASF sample crystals do not have a regular and orderly microstructure, and the particles are mostly agglomerated. After calcination at 200 °C, PG lost its bound water, but the crystal morphology of the sample did not change significantly, and it was still irregularly and chaotically distributed, and the particles were agglomerated. After calcination at 800 °C, the crystal distribution in the sample becomes orderly, and crystal particles with regular morphology appear. After calcination at 1200 °C, well-defined polygonal crystals of $C_4A_3\overline{S}$ were observed, which was confirmed by EDS analysis, indicating the formation of the target mineral.

3.6. Kinetic analysis for PG decomposition in mineral formation

For thermal analysis of non-homogeneous and linear programmed heating, the Arrhenius equation is employed to describe the relationship between the reaction rate constant (k) and the thermodynamic temperature (T). The degree of reaction is expressed in terms of conversion rate (α). Therefore, the integral expression $G(\alpha)$ for reaction kinetics equations can be obtained based on the basic principles of thermal analysis kinetics. The most probable mechanism function can be determined using the Universal Integration Method from many mechanism functions in thermal analysis kinetics. Meanwhile, the activation energy (E) and pre-exponential factor (A) are also calculated [48]. Table 4 lists the common kinetic mechanism functions for solid-phase thermal decomposition considered in this study.

According to the experimental conditions, the heating rate (β) is 10 $K\cdot min^{-1}$, and the universal gas constant (R) is 8.314 $J\cdot mol^{-1}\cdot K^{-1}$. The initial temperature for PG decomposition was observed at approximately 1243.15 K for the PG0 sample, while the PGASF sample exhibited a lower decomposition initiation temperature of about 1152.15 K. According to the TG data of PG and PGASF samples, the conversion rate α can be calculated using the following formula.

$$\alpha = \frac{W_0 - W_t}{W_0 - W_\infty}$$

where, W_0 is the initial mass of the sample, W_t is the mass of the sample at t moment, and W_∞ means terminal sample weight.

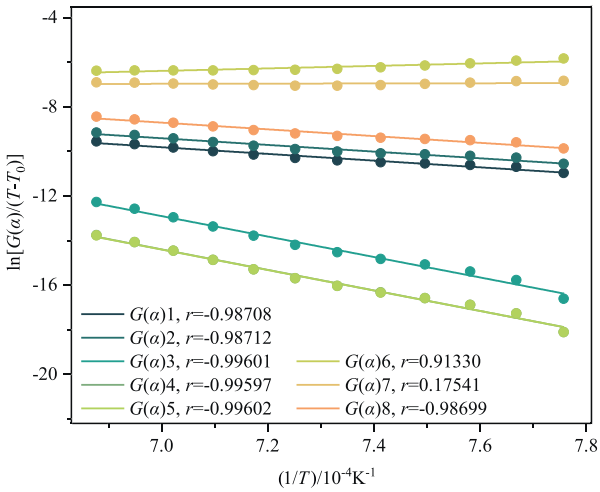


Fig. 9. Decomposition kinetic mechanism function judgment of PG in the PG0 sample.

Fig. 9 shows the linear regression results of $\ln[G(\alpha)/(T-T_0)]$ and $1/T$ for PG decomposition in the PG0 sample, where the numbering and expression of $G(\alpha)$ are shown in Table 4. For $G(\alpha)_5$, the absolute value of the correlation coefficient (r) is the highest, which means that the linear relationship between $\ln[G(\alpha)_5/(T-T_0)]$ and $1/T$ is the best. According to the slope and interception of the fitted line, the kinetic parameters including E and A were obtained. The calculated value of E is 381.75 $kJ\cdot mol^{-1}$, and A is equivalent to $5.07 \times 10^8\ S^{-1}$. Therefore, the decomposition kinetic mechanism of PG is three-dimensional diffusion reaction, and the expression of $G(\alpha)$ is $(1-2\alpha/3)-(1-\alpha)^{2/3}$. Fig. 10 presents the linear regression

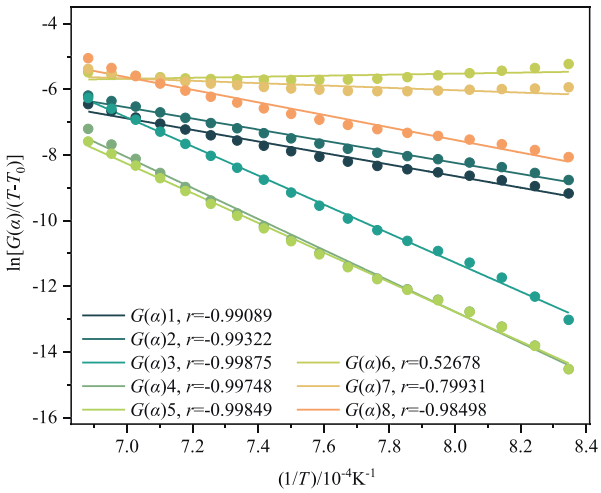


Fig. 10. Decomposition kinetic mechanism function judgment of PG in the PGASF sample.

Table 4
Common kinetic mechanism functions for solid-phase thermal decomposition [49].

No.	Function name	Mechanism	$G(\alpha)$
1	Ball contraction	Phase boundary reaction: Spherical symmetry	$1-(1-\alpha)^{1/3}$
2	Shrink cylinder	Phase boundary reaction: Cylindrical symmetry	$1-(1-\alpha)^{1/2}$
3	Valensi equation	Two-dimensional diffusion: Cylindrical symmetry	$\alpha+(1-\alpha)\ln(1-\alpha)$
4	Jander equation	Three-dimensional diffusion: Spherical symmetry	$[1-(1-\alpha)^{1/3}]^2$
5	G–B equation		$(1-2\alpha/3)-(1-\alpha)^{2/3}$
6	Avrami–Erofeev equation	Random nucleation and subsequent growth	$[-\ln(1-\alpha)]^{1/3}$
7	Avrami–Erofeev equation		$[-\ln(1-\alpha)]^{1/2}$
8	Maple single rule		$-\ln(1-\alpha)$

results of $\ln[G(\alpha)/(T-T_0)]$ and $1/T$ for PG decomposition in the PGASF sample. It can be found that the linear relationship between $\ln[G(\alpha)_3/(T-T_0)]$ and $1/T$ is the most well-defined. The calculated value of E is 367.60 kJ ·mol^{-1}, and A is equivalent to 2.90×10^{11} S^{-1}. In conclusion, the decomposition kinetic mechanism of PG is two-dimensional diffusion (cylindrical symmetry) reaction, and the expression of f $G(\alpha)$ is $\alpha+(1-\alpha)\ln(1-\alpha)$. Obviously, the reaction mechanism of PG decomposition changes in mineral formation, accompanied by a decrease in E and an increase in A, which usually indicates that mineral formation actively promotes and accelerates the decomposition of PG.

4. Conclusions

This study investigated the decomposition of PG and formation of minerals in the preparation of SAC. Compared with the direct decomposition of $CaSO_4$, the mineral formation processes involving $CaSO_4$ decomposition in SAC are more likely to occur spontaneously. The incorporation of $CaSO_4$ and CaO into the formation of SAC minerals accelerates the decomposition of PG. Due to the generation of mineral phases, the decomposition temperature of PG decreases by approximately 100 °C. Among the SAC minerals, the formation of C_2S exhibits the strongest promoting effect on PG decomposition, although excessive liquid phase formation at 1300 °C may lead to partial melting of the system. The formation of $C_4A_3\overline{S}$ shows a weaker promoting effect. In contrast, the formation of C_4AF and complex mineral phases not only enhances the efficient decomposition of PG but also maintains system stability and prevents melting. The highest PG decomposition rate of 86.70% is achieved at 1300 °C. Minerals such as $C_4A_3\overline{S}$, CS, and C_2AS form below 1150 °C, effectively promoting the decomposition of PG during the initial phase. Minerals like CA, C_2S, C_2F, and C_4AF form above 1200 °C, thereby facilitating decomposition of PG in the subsequent phase. The formation of SAC minerals is also affected by the PG decomposition, which makes it difficult to achieve complete conversion to the target mineral. The kinetic mechanism of PG decomposition is three-dimensional diffusion reaction, while the mechanism changes to two-dimensional diffusion (cylindrical symmetry) reaction in mineral formation.

This work reveals the promoting effect of SAC mineral formation on the decomposition of PG, providing important theoretical support and insights for the innovative recovery of Ca and S resources in PG. It remains unclear whether mineral formation indirectly affects PG decomposition by consuming CaO or directly promotes PG decomposition through direct reactions with $CaSO_4$. Therefore, further research is needed to clarify the specific reaction pathways.

CRediT Authorship Contribution Statement

Shuang Wu: Writing – original draft, Visualization, Validation, Software, Project administration, Methodology, Investigation. Changzai Ren: Writing – original draft. Xingliang Yao: Writing – original draft. Yonggang Yao: Writing – review & editing. Wenlong Wang: Conceptualization.

Declaration of Competing Interest

The authors declare that they have no known competing financial interests or personal relationships that could have appeared to influence the work reported in this paper.

Acknowledgments

The authors acknowledge the support of the National Natural Science Foundation of China(52400182), Natural Science Foundation of Shandong Province (ZR2024ME111), Fund of Central Government for Guiding Local Science and Technology Development (YDZX2025021), and Central Guidance for Local Scientific and Technological Development fund project in Xinjiang Uygur Autonomous Region (ZYYD20260Y31).

References

[1] L.A.R. Valle, S.L. Rodrigues, S.J. Ramos, H.S. Pereira, D.C. Amaral, J.O. Siqueira, L.R.G. Guilherme, Beneficial use of a by-product from the phosphate fertilizer industry in tropical soils: effects on soil properties and maize and soybean growth, *J. Clean. Prod.* 112 (2016) 113–120.
[2] R.B. El Zrelli, S. Fabre, S. Castet, M. Grégoire, O. Fersi, C. Josse, A.M. Cousin, P. Courjault-Radé, Unveiling the organic nature of phosphogypsum foam: insights into formation dynamics, pollution load, and contribution to marine pollution in the Southern Mediterranean Sea, *J. Hazard. Mater.* 480 (2024) 135732.
[3] L.F. Lu, T. Tian, R.F. Jin, Q.Y. Ji, J.T. Zhou, Recovery of calcium and sulphur from phosphogypsum with zero by-product generation using a preparative vertical-flow electrophoresis system, *Sep. Purif. Technol.* 331 (2024) 125579.
[4] F. Akfas, A. Elghali, A. Aboulaich, M. Munoz, M. Benzaazoua, J.L. Bodinier, Exploring the potential reuse of phosphogypsum: a waste or a resource, *Sci. Total Environ.* 908 (2024) 168196.
[5] S.J. Zheng, M.S. Chen, T.L. Liu, G.K. Yang, G.S. Jiang, H.M. Gu, Research on compressive strength and thermal conductivity of lightweight phosphogypsum-based composite cementitious materials, *Constr. Build. Mater.* 436 (2024) 136955.
[6] S. Oubaha, Y. Taha, M. Loutou, M. Oualid Mghazli, M. Benzaazoua, R. Hakkou, Fired brick production using phosphogypsum and phosphate mining waste, *Constr. Build. Mater.* 403 (2023) 133149.
[7] M.X. Zhao, X.D. Li, J.X. Yu, F. Li, L. Guo, G.P. Song, C.Q. Xiao, F. Zhou, R. Chi, G. Q. Feng, Highly efficient recovery of phosphate and fluoride from phosphogypsum leachate: selective precipitation and adsorption, *J. Environ. Manag.* 367 (2024) 122064.
[8] S. Zhang, J.Y. Liu, J.W. Ding, M.Y. Gao, C.R. Xue, Effect of recycled phosphogypsum and calcium aluminate cement on the strength behavior optimization of cement-treated dredged soil: a co-utilization of solid wastes, *J. Environ. Manag.* 353 (2024) 120020.
[9] T. Feng, M.J. Huo, X.Q. Zhao, T. Wang, X. Xia, C.Y. Ma, Reduction of SO_2 to elemental sulfur with H_2 and mixed H2/CO gas in an activated carbon bed, *Chem. Eng. Res. Des.* 121 (2017) 191–199.
[10] P.X. Yuan, M. Li, S.Y. Chen, W.G. Xiang, Advances in phosphogypsum calcination and decomposition processes in circulating fluidized beds, *ACS Omega* 9 (38) (2024) 39307–39325.
[11] J.D. Ma, J.Z. Xu, C.H. Liu, Q. Yi, M. Zheng, L.M. Cheng, T. Song, Chemical looping combustion of sulfur paste to SO_2 by phosphogypsum oxygen carrier for sulfur acid production, *Fuel* 323 (2022) 124386.
[12] F.Y. Li, Y.H. Wang, J.B. Liu, Y.X. Li, Z.M. Li, Synthesis, insecticidal evaluation and mode of action of novel anthranilic diamide derivatives containing sulfur moiety as potential ryanodine receptor activators, *Bioorg. Med. Chem.* 27 (5) (2019) 769–776.
[13] S. Liu, C.R. Yang, T.F. Zhang, W. Liu, F. Jiao, W.Q. Qin, Effective recovery of calcium and sulfur resources in FGD gypsum: insights from the mechanism of reduction roasting and the conversion process of sulfur element, *Sep. Purif. Technol.* 314 (2023) 123537.
[14] Q. Wang, X.J. Lyu, Q. Liu, X. Liu, W.T. Zhou, Recycle of soda waste sludge as the limestone material for Portland cement: chemical composition, physical properties and hydration mechanism, *Constr. Build. Mater.* 422 (2024) 135790.
[15] N. Ijaz, W.M. Ye, Z.U. Rehman, Z. Ijaz, Novel application of low carbon limestone calcined clay cement (LC3) in expansive soil stabilization: an eco-efficient approach, *J. Clean. Prod.* 371 (2022) 133492.
[16] D. Silva, C. Weber, C. Oliveira, Neutralization and uptake of pollutant cations from acid mine drainage (amd) using limestones and zeolites in a pilot-scale passive treatment system, *Miner. Eng.* 170 (2021) 107000.
[17] J. Lim, H. Cho, J. Kim, Optimization of wet flue gas desulfurization system using recycled waste oyster shell as high-grade limestone substitutes, *J. Clean. Prod.* 318 (2021) 128492.
[18] P.J. Xu, W.H. Liu, H. Li, Y.X. Chen, Thermal decomposition mechanism and characterization of phosphogypsum in suspension under multifactor coupling effect, *Case Stud. Constr. Mater.* 20 (2024) e02861.
[19] D. Ma, Q.H. Wang, Z.H. Tian, B. Zhang, G.L. Xie, Recovery of sulphur dioxide by converter dust synergistic coke decomposition of phosphogypsum, *Chem. Eng. Sci.* 288 (2024) 119814.

[20] J. Yang, S.L. Dong, L.P. Ma, Q.X. Dai, D.L. Zheng, B. Huang, M.Y. Sun, B. Hu, W. Du, L.G. Xie, L. Duan, X. Yan, Review on high-value utilization of phosphogypsum: utilization of calcium and oxygen resources present in phosphogypusm, *Sep. Purif. Technol.* 344 (2024) 127246.
[21] X.D. Yan, L.P. Ma, B. Zhu, D.L. Zheng, Y. Lian, Reaction mechanism process analysis with phosphogypsum decomposition in multiatmosphere control, *Ind. Eng. Chem. Res.* 53 (50) (2014) 19453–19459.
[22] H.W. He, L.F. Hao, C.G. Fan, S.G. Li, W.G. Lin, A two-step approach to phosphogypsum decomposition: oxidation of CaS with CO_2, *Thermochim. Acta* 708 (2022) 179122.
[23] N. Mihara, D. Kuchar, Y. Kojima, H. Matsuda, Reductive decomposition of waste gypsum with SiO_2, Al_2O_3, and Fe_2O_3 additives, *J. Mater. Cycles Waste Manag.* 9 (1) (2007) 21–26.
[24] J. Yang, B. Zhu, L.P. Ma, H.P. Liu, Investigation of Al_2O_3 and Fe_2O_3 transmission and transformation during the decomposition of phosphogypsum, *Chin. J. Chem. Eng.* 27 (5) (2019) 1125–1131.
[25] L.J. Zhao, T.M. Wan, X.S. Yang, L. Yang, X.J. Kong, Z.Y. Zhang, X.L. Wang, Effects of kaolinite addition on the melting characteristics of the reaction between phosphogypsum and CaS, *J. Therm. Anal. Calorim.* 119 (3) (2015) 2119–2126.
[26] S. Wu, X.L. Yao, C.Z. Ren, Y.G. Yao, W.L. Wang, Recycling phosphogypsum as a sole calcium oxide source in calcium sulfoaluminate cement and its environmental effects, *J. Environ. Manag.* 271 (2020) 110986.
[27] S. Wu, X.L. Yao, C.Z. Ren, Y.G. Yao, C. Zhang, C.L. Wu, W.L. Wang, Effect of iron on the preparation of iron-rich calcium sulfoatablluminate cement using gypsum as the sole calcium oxide source and its incorporation into mineral phases, *Constr. Build. Mater.* 290 (2021) 123214.
[28] S. Wu, Y.G. Yao, X.L. Yao, C.Z. Ren, J.W. Li, D. Xu, W.L. Wang, Co-preparation of calcium sulfoaluminate cement and sulfuric acid through mass utilization of industrial by-product gypsum, *J. Clean. Prod.* 265 (2020) 121801.
[29] C.Q. Zhang, P. Chen, J.Z. Wei, Z.J. Ouyang, W.X. Lv, Effect of different calcination temperatures on clinker and hydration properties of solid waste-based calcium sulfoaluminate cement, *Constr. Build. Mater.* 452 (2024) 138938.
[30] Y. Shen, J.S. Qian, J.Q. Chai, Y.Y. Fan, Calcium sulphoaluminate cements made with phosphogypsum: production issues and material properties, *Cem. Concr. Compos.* 48 (2014) 67–74.
[31] A. Kirfel, G. Will, Charge density in anhydrite, $CaSO_4$, from X-ray and neutron diffraction measurements, *Acta Crystallogr. B* 36 (12) (1980) 2881–2890.
[32] S. John Louisnathan, Refinement of the crystal structure of a natural gehlenite, Ca_2 Al(Al, Si) 2 O_7, *Can. Mineral.* 10 (1971) 822–837.
[33] R.M. Hazen, L.W. Finger, R.J. Hemley, H.K. Mao, High-pressure crystal chemistry and amorphization of α-quartz, *Solid State Commun.* 72 (5) (1989) 507–511.
[34] J. Berggren, O. Foss, I. Roti, H. Okinaka, K. Kosuge, S. Kachi, Refinement of the crystal structure of dicalcium ferrite, $Ca_2Fe_2O_5$, *Acta Chem. Scand.* 25 (1971) 3616–3624.
[35] W. Hörkner, H. Müller-Buschbaum, Zur kristallstruktur von $CaAl_2O_4$, *J. Inorg. Nucl. Chem.* 38 (5) (1976) 983–984.
[36] H. Saalfeld, W. Depmeier, Silicon-free compounds with sodalite structure, *Krist. Tech.* 7 (1–3) (1972) 229–233.
[37] T. Yamanaka, H. Mori, The structure and polytypes of α-$CaSiO_3$ (pseudowollastonite), *Acta Crystallogr. B* 37 (5) (1981) 1010–1017.
[38] W. Mumme, R.J. Hill, G. Bushnell-Wye, A.K. Aride, J.E. Jørgensen, Rietveld crystal structure refinement, crystal chemistry and calculated powder diffraction data for the polymorphs of dicalcium silicate and related phases, *Neues Jahrbuch Mineral. Abhand.* 169 (1995) 35–68.
[39] A.A. Colville, S. Geller, The crystal structure of brownmillerite, $Ca_2FeAlO5$, *Acta Crystallogr. B* 27 (12) (1971) 2311–2315.
[40] J.R. Castillo-Sánchez, K. Oishi, L. St-Germain, D. Ait-Amer, J.P. Harvey, The power of computational thermochemistry in high-temperature process design and optimization: part 1: unit operations, *Calphad* 82 (2023) 102593.
[41] I.C. Popovici, S. Dobrinaş, A. Soceanu, V. Popescu, G. Prodan, I. Omer, New approaches for Pb(II) removal from aqueous media using nanopowder sodium titanosilicate: kinetics study and thermodynamic behavior, *Int. J. Mol. Sci.* 24 (18) (2023) 13789.
[42] C.W. Bale, E. Bélisle, P. Chartrand, S.A. Decterov, G. Eriksson, A.E. Gheribi, K. Hack, I.H. Jung, Y.B. Kang, J. Melançon, A.D. Pelton, S. Petersen, C. Robelin, J. Sangster, P. Spencer, M.A. Van Ende, FactSage thermochemical software and databases, 2010–2016, *Calphad* 54 (2016) 35–53.
[43] P.J. Xu, H. Li, Y.X. Chen, Experimental study on optimization of phosphogypsum suspension decomposition conditions under double catalysis, *Materials* 14 (5) (2021) 1120.
[44] H.L. Liu, Y. Zhang, X.X. Lv, M.S. Cui, K.P. Cui, Z.L. Dai, B. Wang, R. Weerasooriya, X. Chen, Efficient degradation of sulfamethoxazole by diatomite-supported hydroxyl-modified UIO-66 photocatalyst after calcination, *Nanomaterials* 13 (24) (2023) 3116.
[45] B.G. Ma, W.D. Lu, Y. Su, Y.B. Li, C. Gao, X.Y. He, Synthesis of α-hemihydrate gypsum from cleaner phosphogypsum, *J. Clean. Prod.* 195 (2018) 396–405.
[46] L.P. Ma, X.K. Niu, J. Hou, S.C. Zheng, W.J. Xu, Reaction mechanism and influence factors analysis for calcium sulfide generation in the process of phosphogypsum decomposition, *Thermochim. Acta* 526 (1–2) (2011) 163–168.
[47] R. Roy, T. Hertel, A. Muhammad, Y. Pontikes, A methodology to enhance ye'elimite in calcium sulfo-aluminate ferrite clinker from bauxite residue, *Constr. Build. Mater.* 446 (2024) 137968.
[48] S. Vyazovkin, A.K. Burnham, J.M. Criado, L.A. Pérez-Maqueda, C. Popescu, N. Sbirrazzuoli, ICTAC Kinetics Committee recommendations for performing kinetic computations on thermal analysis data, *Thermochim. Acta* 520 (1–2) (2011) 1–19.
[49] Z.Q. Yan, Z.A. Wang, H. Liu, Y.J. Tu, W. Yang, H.C. Zeng, J.R. Qiu, Decomposition and solid reactions of calcium sulfate doped with SiO_2, Fe_2O_3 and Al_2O_3, *J. Anal. Appl. Pyrolysis* 113 (2015) 491–498.